The Fourier Transform of the Continuous Gravitational Wave Signal

S.R. Valluri,[1, a] Vladimir Dergachev,[2, 3, b] X. Zhang,[4, c] and F.A. Chishtie[5, d]

[1] *Department of Physics and Astronomy, The University of Western Ontario, London, ON N6A 3K7, Canada*
[2] *Max Planck Institute for Gravitational Physics (Albert Einstein Institute), Callinstrasse 38, 30167 Hannover, Germany*
[3] *Leibniz Universität Hannover, D-30167 Hannover, Germany*
[4] *Department of Statistical and Actuarial Sciences,*
The University of Western Ontario, London, ON N6A 3K7, Canada
[5] *Department of Applied Mathematics, The University of Western Ontario, London, ON N6A 3K7, Canada*

The direct detection of continuous gravitational waves from pulsars is a much anticipated discovery in the emerging field of multi-messenger gravitational wave (GW) astronomy. Because putative pulsar signals are exceedingly weak large amounts of data need to be integrated to achieve desired sensitivity. Contemporary searches use ingenious ad-hoc methods to reduce computational complexity. In this paper we provide analytical expressions for the Fourier transform of realistic pulsar signals. This provides description of the manifold of pulsar signals in the Fourier domain, used by many search methods. We analyze the shape of the Fourier transform and provide explicit formulas for location and size of peaks resulting from stationary frequencies.

I. INTRODUCTION

Continuous gravitational waves are an eagerly anticipated but elusive phenomena. Despite a series of searches since early 2000 (in particular [1–7]) there have been no loud detections. Some recent papers have seen signals with moderately high SNR, but it is not known yet whether they are due to the instrumental noise or astrophysical signals.

Continuous gravitational waves are expected from rapidly rotating neutron stars, as well as from more exotic sources [8–13].

In this paper we study the Fourier transform of the continuous wave signal using analytical techniques. Our results are useful for developing loosely coherent algorithms [14–16] which adapt to the shape of the signal manifold.

We provide explicit formulas describing location and strength of the peaks in the Fourier transform. Such peaks increase signal susceptibility to detector artifacts. An analysis of a signal can be performed by correlating peak locations with likely frequencies of instrumental lines. The algorithm for peak computation is detailed in figure 4.

II. SIGNAL MODEL

A pure monochromatic signal has linear phase evolution. While this would be computationally simple to search for, the search would be challenging due to confusion of putative signals with numerous instrumental lines [5].

Realistic gravitational wave signals have multiple sources of modulation, due to Doppler shifts from detector motion relative to the source, possible source motion due to nearby astrophysical bodies, or intrinsic evolution of the source, such as slow decrease in frequency due to energy loss.

All such signals are nearly monochromatic and can be described by the equation

$$h(t) = \Re(a(t)e^{i\phi(t)}) \tag{1}$$

The amplitude modulation $a(t)$ varies slowly compared to rapid oscillations of the exponential terms. To simplify exposition we assume that $a(t)$ is unity everywhere the signal is defined. This allows us to focus on the oscillatory nature of our signal, while still allowing a measure of amplitude modulation by introducing gaps in input data.

Such gaps occur naturally due to lock losses in interferometer operations. They can also arise effectively in data that would normally be deweighted due to high noise, or due to unfavorable interferometer angle to incoming linearly polarized signal.

The phase modulation $\phi(t)$ is a powerful tool in separating astrophysical signals from detector artifacts, but its complicated form and dependence on many parameters, such as source and detector locations and frequency drift parameters presents a computational challenge.

It is instructive to consider a simplified situation of a fixed frequency source and a detector following two superimposed circular motions - one around Earth's axis and one of Earth around the Sun.

First, we compute relative detector position to Earth center:

$$\vec{r}_{\text{Earth}} = \begin{pmatrix} \cos(\omega_{\text{rot}}t + \alpha_0)\cos(\delta_0) \\ \sin(\omega_{\text{rot}}t + \alpha_0)\cos(\delta_0) \\ \sin(\delta_0) \end{pmatrix} R_{\text{Earth}} \tag{2}$$

where α_0 and δ_0 are the detector longitude and latitude locations correspondingly.

The full motion of the detector is then described as

$$\vec{r}_{\text{det}} = \vec{r}_{\text{Earth}} + \vec{v}\cos(\omega_{\text{orb}}t) + \vec{u}\sin(\omega_{\text{orb}}t) \qquad (3)$$

where $\vec{u}$ and $\vec{v}$ are two perpendicular vectors in the ecliptic plane parametrizing Earth's orbital motion.

This can be generalized as

$$\vec{r}_{\text{det}} = \vec{r}_{\text{off}} + \sum_{k=1}^{K} \vec{v}_k\cos(\omega_k t) + \vec{u}_k\sin(\omega_k t) \qquad (4)$$

Here $\vec{r}_{\text{off}}$ is a constant offset, which for circular approximation is $R_{\text{Earth}}\sin(\delta_0)\hat{\vec{z}}$. Since the offset is constant, it only affects absolute signal phase. For simplicity we will assume $\vec{r}_{\text{off}} = 0$ in subsequent calculations.

Our simplified example with two modulations arising from circular motions corresponds to $K = 2$. The expression 4 is general enough that one can fit any realistic signal by including additional harmonics, for example, due to planetary perturbations.

The direction to the source is given by

$$\hat{n}_{\text{source}} = \begin{pmatrix} \cos(\alpha)\cos(\delta) \\ \sin(\alpha)\cos(\delta) \\ \sin(\delta) \end{pmatrix} \qquad (5)$$

Here α is the right ascension in radians $[0, 2\pi)$ and δ is the declination in radians $[-\pi/2, \pi/2]$.

The detector velocity vector is

$$\vec{v}_{\text{det}} = \frac{d}{dt}\vec{r}_{\text{det}} = \sum_{k=1}^{K} \vec{u}_k\omega_k\cos(\omega_k t) - \vec{v}_k\omega_k\sin(\omega_k t) \qquad (6)$$

The Doppler shift is computed from the formula:

$$\begin{aligned} \mathcal{D} &= \frac{\hat{n}_{\text{source}} \cdot \vec{v}_{\text{det}}}{c} \\ &= \sum_k \frac{\hat{n}_{\text{source}} \cdot \vec{u}_k}{c}\omega_k\cos(\omega_k t) - \frac{\hat{n}_{\text{source}} \cdot \vec{v}_k}{c}\omega_k\sin(\omega_k t) \end{aligned} \qquad (7)$$

We introduce relative modulation depth a_k^{rel} and modulation phase ϕ_k:

$$a_k^{\text{rel}} = \frac{\omega_k}{c}\sqrt{(\hat{n}_{\text{source}} \cdot \vec{u}_k)^2 + (\hat{n}_{\text{source}} \cdot \vec{v}_k)^2} \qquad (8)$$

$$\phi_k = \arctan\left(\frac{\hat{n}_{\text{source}} \cdot \vec{u}_k}{\hat{n}_{\text{source}} \cdot \vec{v}_k}\right) \qquad (9)$$

Then the Doppler shift becomes:

$$\mathcal{D} = \sum_{k=1}^{K} a_k^{\text{rel}}\cos(\omega_k t + \phi_k) \qquad (10)$$

Let us widen the model for our source signal to include polynomial frequency evolution, which is observed in radio pulsars:

$$f(t) = \sum_{n=0}^{N} f_n\frac{t^n}{n!} \qquad (11)$$

The signal received at the detector is then

$$f(t) = \left(\sum_{n=0}^{N} f_n\frac{t^n}{n!}\right)\left(1 + \sum_{k=1}^{K} a_k^{\text{rel}}\cos(\omega_k t + \phi_k)\right) \qquad (12)$$

This ignores relativistic corrections.

Let us assume that the products $f_n a_k^{\text{rel}}$ are negligible for all $n \geq 1$. Then the signal model simplifies to:

$$f(t) = \sum_{n=0}^{N} f_n\frac{t^n}{n!} + f_0\sum_{k=1}^{K} a_k^{\text{rel}}\cos(\omega_k t + \phi_k) \qquad (13)$$

We now introduce phase modulation depth a_k as

$$a_k = \frac{2\pi f_0 a_k^{\text{rel}}}{\omega_k} = \frac{2\pi f_0}{c}\sqrt{(\hat{n}_{\text{source}} \cdot \vec{u}_k)^2 + (\hat{n}_{\text{source}} \cdot \vec{v}_k)^2} \qquad (14)$$

Then the phase model of our signal is

$$\phi(t) = \phi_0 + 2\pi\sum_{n=1}^{N} f_{n-1}\frac{t^n}{n!} + \sum_{k=1}^{K} a_k\sin(\omega_k t + \phi_k) \qquad (15)$$

Here ϕ_0 controls the initial phase of the signal.

To make sense of modulation amplitudes and phases, we focus on our initial case of two circular modulations.

The vectors u_1 and v_1 describing Earth's rotation are

$$\vec{v}_1 = R_{\text{Earth}}\begin{pmatrix} \cos\alpha_0\cos\delta_0 \\ \sin\alpha_0\cos\delta_0 \\ 0 \end{pmatrix} \qquad (16)$$

$$\vec{u}_1 = R_{\text{Earth}}\begin{pmatrix} -\sin\alpha_0\cos\delta_0 \\ \cos\alpha_0\cos\delta_0 \\ 0 \end{pmatrix} \qquad (17)$$

where α_0 and δ_0 are detector longitude and latitude correspondingly.

Then the parameters corresponding to Earth's rotation are

$$\begin{aligned} \phi_1 &= \arctan\left(\frac{\hat{n}_{\text{source}} \cdot \vec{u}_k}{\hat{n}_{\text{source}} \cdot \vec{v}_k}\right) = \\ &= \arctan\left(\frac{\sin(\alpha-\alpha_0)\cos(\delta_0)}{\cos(\alpha-\alpha_0)\cos(\delta_0)}\right) = \alpha - \alpha_0 \end{aligned} \qquad (18)$$

$$a_1 = \frac{2\pi f_0 R_{\text{Earth}}}{c}|\cos(\delta)\cos(\delta_0)| \qquad (19)$$

We see that modulation phase ϕ_1 is just the difference between source right ascension and detector longitude.

The vectors u_2 and v_2 describing Earth orbital motion are

$$\vec{v}_2 = R_{\text{orb}}\begin{pmatrix} 1 \\ 0 \\ 0 \end{pmatrix} \qquad (20)$$

$$\vec{u}_2 = R_{\text{orb}}\begin{pmatrix} 0 \\ \cos\epsilon \\ \sin\epsilon \end{pmatrix} \qquad (21)$$

where $\epsilon = 23.4°$ is the obliquity of the ecliptic

The parameters corresponding to Earth orbital motion around the Sun are somewhat more complicated:

$$\phi_2 = \arctan\left(\frac{\sin(\alpha)\cos(\delta)\cos(\epsilon) + \sin(\delta)\sin(\epsilon)}{\cos(\alpha)\cos(\delta)}\right) \quad (22)$$

$$a_2 = \frac{2\pi f_0 R_{\text{orb}}}{c} \cdot$$
$$\cdot \sqrt{\cos^2(\alpha)\cos^2(\delta) + (\sin(\alpha)\cos(\delta)\cos(\epsilon) + \sin(\delta)\sin(\epsilon))^2} \quad (23)$$

This complexity is due to the choice of equatorial coordinate system. Had we chosen ecliptic coordinates instead the orbital motion parameters would be simple, while the Earth rotation parameters have similar expressions to the above. As we will see later the shorter period motion introduces more complexity in the Fourier transform, so it makes sense to use the equatorial coordinate system in applications.

III. FOURIER TRANSFORM OF QUASI-MONOCHROMATIC SIGNAL

In the general case the signal spectrum is

$$\tilde{h}_0(f) = \int_{-T/2}^{T/2} \exp\left(i\phi(t)\right) e^{-i2\pi ft} dt =$$
$$= \int_{-T/2}^{T/2} \exp\left\{i\phi_0 + 2\pi i \sum_{n=2}^{N} f_{n-1}\frac{t^n}{n!} + \right.$$
$$\left. + i\sum_{k=1}^{K} a_k \sin(\omega_k t + \phi_k)\right\} \cdot e^{-i2\pi(f-f_0)t} dt \quad (24)$$

Thus the spectrum depends on initial signal phase ϕ_0, initial frequency f_0, higher order frequency expansion parameters f_k (for $k \geq 1$), phase modulation depth a_k and modulation phase ϕ_k.

For searches less than 30 days the effect of third order and higher frequency derivatives can be neglected for astrophysical sources. Keeping terms up to a second order in frequency, the equation simplifies to

$$\tilde{h}_0(f) = \int_{-T/2}^{T/2} \exp\left\{i\phi_0 + i2\pi\left(f_1\frac{t^2}{2} + f_2\frac{t^3}{6}\right) + \right.$$
$$\left. + i\sum_{k=1}^{K} a_k \sin(\omega_k t + \phi_k)\right\} \cdot e^{-i2\pi(f-f_0)t} dt \quad (25)$$

The treatment of sinusoidal phase modulation can use either the Jacobi-Anger expansion in terms of Bessel functions or approximation of the sine function by polynomials. The latter is particularly effective when $\omega_l T$ is small.

For example:

$$a_k \sin(\omega_k t + \phi_k) = a_k\left(\omega_k t - \frac{\omega_k^3 t^3}{6} + O(\omega_k^5 t^5)\right)\cos(\phi_k) +$$
$$+ a_k\left(1 - \frac{\omega_k^2 t^2}{2} + O(\omega_k^4 t^4)\right)\sin(\phi_k)) \quad (26)$$

Modulation term	Source frequency	Earth rotation	Orbital motion	Unit
ω_l	-	6.3	0.017	(1/day)
a_l	200 Hz	23	630000	-
a_l	1000 Hz	115	3200000	-
a_l	2000 Hz	230	6300000	-
$a_l\omega_l$	200 Hz	0.0017	0.123	Hz
$a_l\omega_l$	1000 Hz	0.0084	0.63	Hz
$a_l\omega_l$	2000 Hz	0.017	1.23	Hz
$a_l\omega_l^2$	200 Hz	1.2×10^{-7}	2.4×10^{-8}	Hz^2
$a_l\omega_l^2$	1000 Hz	6.1×10^{-7}	1.2×10^{-7}	Hz^2
$a_l\omega_l^2$	2000 Hz	1.2×10^{-6}	2.4×10^{-7}	Hz^2

TABLE I: Modulation parameters

Modulation parameters for various sources. The amplitude modulation values are worst case, as seen in LIGO Livingston interferometer. Phase and frequency modulation are dominated by orbital motion, while the frequency derivatives are larger for terms from Earth rotation.

Table I shows modulation parameters for sources emitting at various example frequencies.

For example, in the case of $T = 3$ days we find that the Earth's orbital motion is a good candidate for polynomial expansion and would need terms up to a cubic order.

Indeed, the error in equation 26 can be bounded by the 4-th order term:

$$a_l \frac{\omega_l^4 T^4}{4! 2^4} \leq 0.11 \quad (27)$$

Here we assumed the expansion is centered on the middle of the interval so the maximum time is $T/2$.

Let L_E be the set of indices describing expanded harmonics. Consider the following integral by neglecting constant phase term:

$$\tilde{h}_0(f) = \int_{-T/2}^{T/2} \exp\left(2\pi i g_1\frac{t^2}{2} + 2\pi i g_2\frac{t^3}{6} + \right.$$
$$\left. + i\sum_{k \notin L_E} a_k \sin(\omega_k t + \phi_k)\right) \cdot e^{-i2\pi(f-g_0)t} dt \quad (28)$$

where coefficients g_n have been introduced that describe both initial polynomial frequency modulation parameters and the contribution from polynomial expansion of sinusoidal modulations:

$$g_n = f_n + \sum_{k \in L_E} \frac{a_k \omega_k^{n+1}}{2\pi(n+1)!} \cos\left(\phi_k + \frac{\pi n}{2}\right) \quad (29)$$

This model of polynomial plus harmonics is very effective in describing a realistic pulsar signal. As we will show

later, the phase behaviour can be approximated with a single harmonic plus a third order polynomial over any data stretch of 3 days or less.

We now focus on the application of the Jacobi-Anger expansion. Applying it to all sinusoidal terms we get:

$$\tilde{h}_0(f) = \int_{-T/2}^{T/2} \exp\left(2\pi i g_1 \frac{t^2}{2} + 2\pi i g_2 \frac{t^3}{6} - i2\pi\left(f - g_0\right)t\right) \cdot$$
$$\cdot \exp\left(i \sum_{l \notin L_E} a_l \sin(\omega_l t + \phi_l)\right) dt =$$
$$= \int_{-T/2}^{T/2} \exp\left(2\pi i g_1 \frac{t^2}{2} + 2\pi i g_2 \frac{t^3}{6} - i2\pi\left(f - g_0\right)t\right) \cdot$$
$$\cdot \prod_{l \notin L_E} \sum_{k_l} i^{k_l} J_{k_l}(a_l) \exp(ik_l(\omega_l t + \phi_l)) dt$$
(30)

The product and sum symbols can be exchanged yielding a sum over multi-indices $\vec{k} = (k_1, \ldots, k_M)$:

$$\tilde{h}_0(f) = \int_{-T/2}^{T/2} \exp\left(2\pi i g_1 \frac{t^2}{2} + 2\pi i g_2 \frac{t^3}{6} - i2\pi\left(f - g_0\right)t\right) \cdot$$
$$\cdot \sum_{\vec{k}} \prod_{l \notin L_E} i^{k_l} J_{k_l}(a_l) \exp(ik_l(\omega_l t + \phi_l)) dt$$
(31)

The indices $\vec{k}$ span an infinite lattice for exact expression. However, the values $J_{k_l}(a_l)$ decrease rapidly for $k_l \gg |a_l|$, allowing a finite sum to be used in practical calculations.

The number of remaining indices in a sum depends on modulation depth a_l and can be fairly substantial even for relatively small modulation values. This complexity is intrinsic to the problem, as can be confirmed by examining numerically computed Fourier transform in figure 2 - the multitude of peaks would need separate harmonic terms to produce them.

Mathematically, this can be understood as follows.

First we perform the expansion of longer period harmonics as done in Equation 28 keeping only one remaining harmonic. Then we split the integral into pieces of length matching one period T_p (where $T_p \omega_1 = 2\pi$). We assume the full integration interval is the integer multiple of period T_p:

$$\tilde{h}_0(f) = \sum_{m=0}^{M} \int_{-T_p/2 + mT_p}^{T_p/2 + mT_p} \cdot$$
$$\cdot \exp\left(2\pi i g_1 \frac{t^2}{2} + 2\pi i g_2 \frac{t^3}{6} + i a_1 \sin(\omega_1 t + \phi_1)\right) \cdot$$
$$\cdot e^{-2\pi i(f-g_0)t} dt$$
(32)

Shifting the internal integration variable by mT_p we obtain:

$$\tilde{h}_0(f) = \sum_{m=0}^{M} \int_{-T_p/2}^{T_p/2} \exp\left(2\pi i g_1 \frac{(t+mT_p)^2}{2} + \right.$$
$$\left. + 2\pi i g_2 \frac{(t+mT_p)^3}{6} + i a_1 \sin(\omega_1 t + \phi_1)\right) \cdot$$
$$\cdot e^{-2\pi i(f-g_0)(t+mT_p)} dt$$
(33)

The argument of the sine function is unmodified because we shift by integral number of periods.

The Taylor formula provides a convenient way to compute a shift of any analytic function:

$$p(t + T) = \sum_{k=0}^{\infty} \frac{T^k}{k!} \frac{d^k}{dt^k} p(t)$$
(34)

For polynomials the sum is finite because higher order derivatives vanish. Our polynomial is only third order:

$$p(t) = 2\pi(g_0 - f)t + 2\pi g_1 \frac{t^2}{2} + 2\pi g_2 \frac{t^3}{6}$$
(35)

Leading to a simple expression for the shift:

$$\begin{aligned} p(t + mT_p) = \ & p(t) + \\ & + mT_p 2\pi(g_0 - f + g_1 t + g_2 \frac{t^2}{2}) + \\ & + \frac{m^2 T_p^2}{2} 2\pi(g_1 + g_2 t) + \\ & + \frac{m^3 T_p^3}{6} 2\pi g_2 \end{aligned}$$
(36)

Thus the shifted integral can be described as a convolution of a single-period Fourier transform with a Fourier transform of $\exp(i(p(t + mT_p) - p(t))$. The latter can be separated into three parts:

- a multiplication by the phase

$$\exp\left(2\pi i \left(\frac{g_1 m^2 T_p^2}{2} + \frac{g_2 m^3 T_p^3}{6}\right)\right)$$
(37)

- a shift in frequency by $g_1 mT + g_2 m^2 T_p^2/2$ which we denote by operator $\mathbb{S}$.

- and a convolution with Fourier transform of a Gaussian $\exp(\pi i T_p g_2 t^2)$ iterated m times. We denote a single iteration of the convolution by operator $\mathbb{T}$.

Then the full integral can be expressed as

$$\tilde{h}_0(f) = \sum_{m=0}^{M} e^{2\pi i \left(\frac{g_1 m^2 T_p^2}{2} + \frac{g_2 m^3 T_p^3}{6}\right)} \mathbb{T}^m \mathbb{S} \tilde{h}_0^1(f)$$
(38)

where $\tilde{h}_0^1(f)$ denotes a single period Fourier transform:

$$\tilde{h}_0^1(f) = \int_{-T_p/2}^{T_p/2} \exp\left(2\pi i g_1 \frac{t^2}{2} + 2\pi i g_2 \frac{t^3}{6} + \right.$$
$$\left. + i a_1 \sin(\omega_1 t + \phi_1)\right) e^{-i2\pi(f-g_0)t} dt$$
(39)

This expression explains features of the Figure 2. The repeated pattern is due to iterations of the operator $\mathbb{T}$. However, both this operator and the frequency shift $\mathbb{S}$ introduce frequency shifts that are not aligned to frequency bins of the full Fourier transform. Thus the height of peaks varies with each iteration.

The variation in phase together with convolution acts to scramble the heights of smaller peaks resulting in a signature of the underlying signal.

IV. FOURIER TRANSFORM SHAPE

The equation 38 allows us to understand the Fourier transform of continuous wave signals in a qualitative way. For practical applications it is desirable to know the details such as location of the peaks and their heights.

While this can be done by the numerical integration of formula 38, the computation is comparable in difficulty to taking the Fourier transform directly. What we would like instead is a simple formula depending on parameters of the signal g_k, ω_1 and ϕ_1.

To obtain such formulas, consider the integral

$$
\tilde{h}_0(f) = \int_{-T/2}^{T/2} \exp\left(2\pi i g_1 \frac{t^2}{2} + 2\pi i g_2 \frac{t^3}{6} + \right.
$$
$$
\left. + i \sum_{l \notin L_E} a_l \sin(\omega_l t + \phi_l) \right) e^{-2\pi i (f - g_0) t} dt = \quad (40)
$$
$$
= \int_{-T/2}^{T/2} \exp\left(i\Lambda(t) \right) dt
$$

Because of the imaginary terms in the exponent it is highly oscillatory. These oscillations will cancel out (on average), except in points where derivative of $\Lambda(t)$ vanishes:

$$
\Lambda'(t) = 2\pi g_1 t + 2\pi g_2 \frac{t^2}{2} + \sum_{l \notin L_E} a_l \omega_l \cos(\omega_l t + \phi_l) - 2\pi \left(f - g_0 \right)
$$
$$
(41)
$$

This can be rewritten as

$$
F(t) = g_0 + g_1 t + g_2 \frac{t^2}{2} + \sum_{l \notin L_E} \frac{a_l \omega_l}{2\pi} \cos(\omega_l t + \phi_l) = f \quad (42)
$$

Because f is a free parameter, the support of the spectrum of our signal is close to the image of the interval $[-T/2, T/2]$ under a function $F(t)$ (Figure 2).

The largest peaks in the spectrum should correspond to the values of f for which larger time intervals have stationary phase, and thus to the points $f_a = F(t_a)$ such that derivative of F vanishes:

$$
F'(t_a) = g_1 + g_2 t_a - \sum_{l \notin L_E} \frac{a_l \omega_l^2}{2\pi} \sin(\omega_l t_a + \phi_l) = 0 \quad (43)
$$

This equation has an approximate solution in the special case of a single sinusoidal term and small parameters g_1 and g_2.

In this case the equation reduces to

$$
\sin(\omega_1 t_a + \phi_1) = \frac{2\pi g_1}{a_l \omega_1^2} + \frac{2\pi g_2}{a_l \omega_1^2} t_a \quad (44)
$$

Let $t_a^0 = \frac{-\phi_1 + \pi n}{\omega_1}$ be the zero of the sine function.

Applying one step of Newton-Raphson method to find the solution of the above equation using t_a^0 as the initial value, we have

$$
t_a = t_a^0 - \frac{g_1 + g_2 t_a^0}{g_2 - (-1)^n \frac{a_1 \omega_1^3}{2\pi}} \quad (45)
$$

Let us check how close we got to true zero of $F'(t)$. We substitute t_a into equation 43:

$$
F'(t_a) = g_1 + g_2 t_a - \frac{a_l \omega_1^2}{2\pi} \sin(\omega_1 t_a + \phi_l) \approx
$$
$$
\approx a_1 \omega_1^2 O\left(\left(-\omega_1 \frac{g_1 + g_2 t_a^0}{g_2 - (-1)^n \frac{a_1 \omega_1^3}{2\pi}} \right)^3 \right) \quad (46)
$$

We see the approximate solution t_a has canceled all linear terms.

To find out the frequencies of the peaks we can now substitute t_a into the Eq. 42. We find

$$
f \approx F(t_a) \approx g_0 + g_1 t_a + g_2 \frac{t_a^2}{2} +
$$
$$
+ (-1)^n \frac{a_1 \omega_1}{2\pi} \left(1 - \frac{1}{2} \left(\frac{\omega_1(g_1 + g_2 t_a^0)}{g_2 - (-1)^n \frac{a_1 \omega_1^3}{2\pi}} \right)^2 \right) \quad (47)
$$

The zeros of the second frequency derivative are simpler to find:

$$
F''(t_a) = g_2 - \sum_{l \notin L_E} \frac{a_l \omega_l^3}{2\pi} \cos(\omega_l t_b + \phi_l) = 0 \quad (48)
$$

In the case of a single sinusoidal term we have:

$$
\frac{a_1 \omega_1^3}{2\pi} \cos(\omega_1 t_b + \phi_1) = g_2 \quad (49)
$$

$$
t_b = \frac{\arccos\left(\frac{2\pi g_2}{a_1 \omega_1^3} \right) - \phi_1 + \pi n}{\omega_1} \quad (50)
$$

For the common case of $|2\pi g_2| \ll |a_1 \omega_1^3|$ the formula simplifies to

$$
t_b = -\phi_1 + \pi n \quad (51)
$$

To test these formulas we generated barycentered time series for LIGO Hanford and Livingston interferometers [17] for multiple sky locations over one year period.

Figure 1 shows locations of local frequency maxima and minima, as well as inflection points where the second frequency derivative vanishes for a portion of this data for a 3-day period starting at GPS time 1160657033 generated for LIGO Hanford interferometer.

Figure 2 shows power spectrum (absolute value squared of the Fourier transform) of a pure 1000 Hz signal with amplitude 1 as observed by LIGO Hanford interferometer. Unlike real data sets which have gaps due to interferometer lock loss this time series is contiguous.
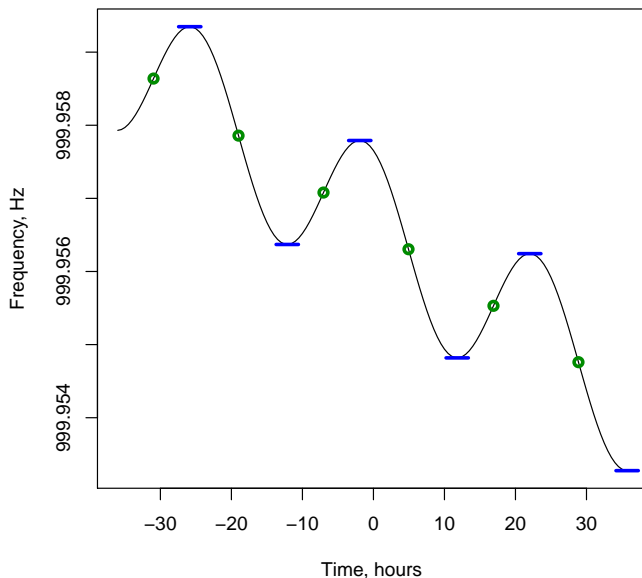
FIG. 1: Example 3-day frequency evolution of $1000\,\mathrm{Hz}$ monochromatic signal from source at right ascension $0°$ and declination $0°$. The blue lines mark locations of local frequency minima and maxima. Green circles mark location of inflection points. The frequencies were computed for LIGO Hanford interferometer. The 3-day segment started at GPS 1160657033.

FIG. 2: Example 3-day Fourier transform of $1000\,\mathrm{Hz}$ monochromatic signal from source at right ascension $0°$ and declination $0°$. The green line at the bottom of the plot shows spectrum support region estimated using equation 42. The blue line at the top shows peak locations estimated using equation 47. The Fourier transform was computed assuming 100% duty cycle for LIGO Hanford interferometer. The 3-day segment started at GPS 1160657033.

We observe that the spectrum support (marked by the thick green line below the graph) is correctly computed by formula 42.

The peak locations marked by short blue lines at the top of the graph were computed with formula 47 and correspond well with numerical results.

Having found peak locations we would like to have a measure of their heights, as those clearly vary.

Near a point of stationary frequency the Fourier transform has the form

$$h_{\mathrm{local}}(f) = \int_{t_0}^{t_1} e^{2\pi i \left(\phi + F(t_a)(t-t_a) + \tilde{g}_2 (t-t_a)^3/6\right)} e^{-2\pi i f t} dt$$

(52)

where we introduced $\tilde{g}_2$:

$$\tilde{g}_2 = g_2 - \frac{a_1}{2\pi} \frac{\cos\left(\omega_1 t_a + \phi_1\right)}{6}$$

(53)

This equation is designed to describe the vicinity of $f = F(t_a)$. The limits of the integration t_0 and t_1 bound the region where the approximation holds, in particular there is no need to integrate over points close to other stationary frequency points.
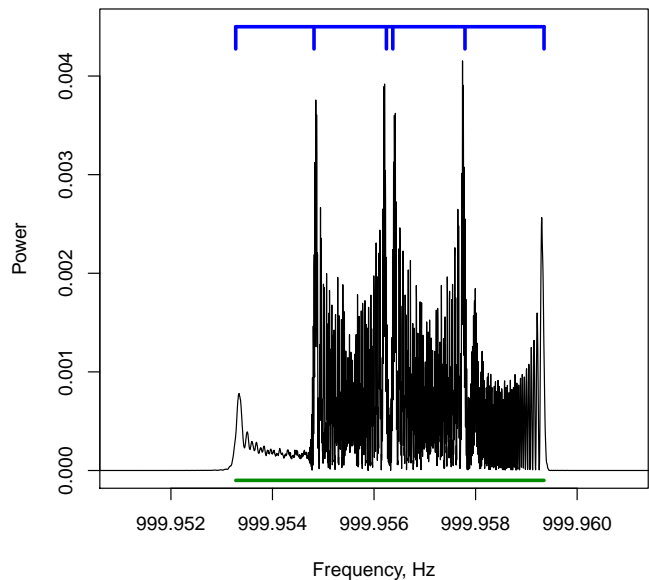
The height of the peak is

$$|h_{\mathrm{local}}(F(t_a))| = \left| \int_{t_0}^{t_1} e^{2\pi i \tilde{g}_2 (t-t_a)^3/6} dt \right|$$

(54)

We now need to find out which values of t_0 and t_1 to use. Naively we might expect that one should use a small interval where the frequency does not change far away from stationary value $F(t_a)$.

However, this will grossly underestimate peak height. The reason is that the value of truncated Airy function (equation 54) keeps growing with increasing time interval, as these pieces contribute due to spectral leakage.

A good heuristic is to choose t_0 and t_1 to be the inflection points, or data boundary if it occurs earlier.

The truncated Airy function has an expression in terms of incomplete Gamma function:

$$\int_{t_0}^{t_1} e^{it^3} dt = \frac{1}{3\sqrt[3]{-i}} \left(\Gamma\left(\frac{1}{3}, -it_0^3\right) - \Gamma\left(\frac{1}{3}, -it_1^3\right) \right)$$

(55)

This equation has some ambiguity as to the branch of cubic roots. This arises purely from using incomplete Γ

function:

$$\Gamma(a, z) = \Gamma(a) \left(1 - z^a e^{-z} \sum_{k=0}^{\infty} \frac{z^k}{\Gamma(a + k + 1)} \right) \quad (56)$$

The constant terms in the formula above subtract when substituted in Eq. 55.

This can also be seen by expanding e^{it^3} into a Taylor series and integrating the result:

$$\int_{t_0}^{t_1} e^{it^3} dt = \sum_{k=0}^{\infty} \frac{i^k t_1^{3k+1}}{k!(3k + 1)} - \sum_{k=0}^{\infty} \frac{i^k t_0^{3k+1}}{k!(3k + 1)} \quad (57)$$

However, for practical application it is convenient to approximate with a heuristic piece-wise linear function that captures the general shape of the integral.

To do this, we introduce the function

$$H(a) = \begin{cases} |a| & \text{when } |a| < 0.4 \\ 0.4 & \text{when } |a| \geq 0.4 \end{cases} \quad (58)$$

Then

$$|h_{\text{local}}(F(t_a))| = \left| \int_{t_0}^{t_1} e^{2\pi i \tilde{g}_2 (t - t_a)^3 / 6} dt \right| \approx$$
$$\approx \frac{1}{\kappa} \left| H(t_1 \kappa) - (-1)^{\text{sgn}(t_0)\text{sgn}(t_1)} H(t_0 \kappa) \right| \quad (59)$$

where $\kappa = \sqrt[3]{6/\tilde{g}_2}$.

This simple formula works surprisingly well. An illustration is given in Figure 3. Here we marked both peak locations and their strength. Also for this example we introduced a gap of 30 hours.

V. SPECTRUM SHAPE ALGORITHM

The analysis detailed in the previous section can be condensed into the algorithm for determining Fourier transform spectral shape (Table 4).

At the start of the algorithm we compute a sequence of times relative to Solar System barycenter. This could be done exactly, or as an approximation. For example, one can compute these times for a relatively coarse grid on the sky and then use a suitable method, such as [18] to interpolate between locations.

Once this time series has been obtained it can be fitted to the formula

$$t_i = \sum_{k=1}^{K} g_k s_i^k + A \cos(\omega_1 s_i + \phi_1) \quad (60)$$

over an interval matching the coherence length of the Fourier transform. Long stretches of data are best analyzed using overlapped intervals. A straightforward speedup is to interpolate the fits from those computed on a coarse grid.

Also, iteration over signal waveforms with the same sky location but with different frequency drift is achieved by direct modifications of coefficients g_k.
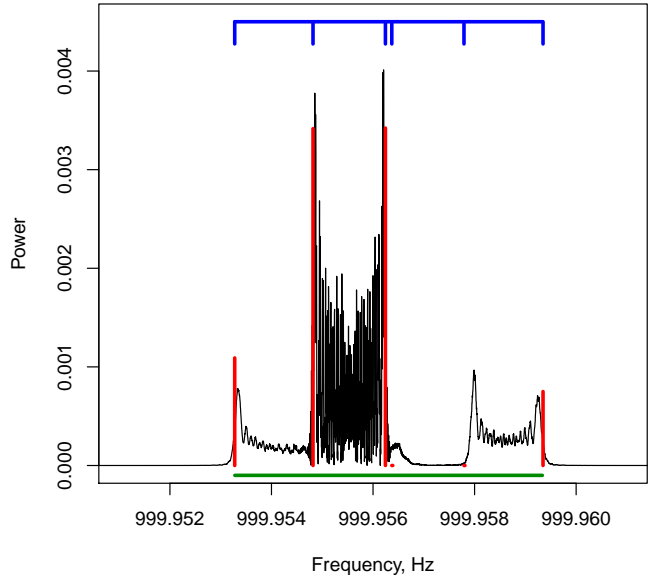

FIG. 3: Example 3-day Fourier transform of 1000 Hz monochromatic signal from source at right ascension $0°$ and declination $0°$. The green line at the bottom of the plot shows spectrum support region estimated using equation 42. The blue line at the top shows peak locations estimated using equation 47. The red lines show peak strength estimated using equation 59. The Fourier transform was computed assuming the data stretch had a 30 hour gap in data for LIGO Hanford interferometer. The 3-day segment started at GPS 1160657033. The gap started 10 hours later.

With the fit in hand, it is straightforward to find locations of stationary points t_a and inflection points t_b (equations 45, 50, 51).

Now the frequencies of the peaks are given by formula 47 and peak height is computed using formula 59.

The computed spectrum shape can be used to understand the dwell time of signal waveform and used to characterize and mitigate the influence of detector artifacts - either after analysis by removing outliers coincident with detector lines, or during the analysis by decreasing weight of segments with larger peak heights.

VI. PERFORMANCE

The formulas 47, 54, 59 are very efficient compared to computing Fourier transform from scratch or to numerically integrating 38.

This efficiency is contingent on the validity of the underlying model. To test how well this model fits the data we made a study using numerically computed timings.

1. The input to the algorithm is a series of timestamps $\{s_i\}_{i=1}^N$ in the local interferometer frame, as well as the computed times $\{t_i\}_{i=1}^N$ in solar system barycenter frame.

2. Compute the fit $t_i = \sum_{k=1}^K g_k s_i^k + A\cos(\omega_1 s_i + \phi_1)$. K can be taken as 3 for time intervals shorter than 3 days. ω_1 is the rotational frequency correspondingly to Earth sidereal period.

3. Compute times of zero frequency derivative and their corresponding stationary frequencies (see equations 45 and 47). These give peak locations.

4. Compute times of zero second frequency derivative (inflection points, equations 50 and 51).

5. Estimate peak amplitudes with formula 59, where t_0 and t_1 are nearest inflection points or data boundaries.

6. The output of the algorithm consists of estimated peak frequencies and amplitudes

FIG. 4: Algorithm used to compute the shape of Fourier transform

A coarse sky grid of 182 points was used for this study. The points on the grid were arranged in $18°$ increments in declination and right ascension. Only one value of right ascension was used for equatorial poles with declination of $\pm 90°$.

For each point in the sky grid we generated 17520 Solar System Barycenter timings using routines from LAL library [19]. The timing started at GPS 1160657033 with 0.5 hour increments. Separate datasets were generated for LIGO Hanford and Livingston interferometers.

Using this dataset we tested fit to single harmonic model:

$$t' = \sum_{k=0}^K g_k \frac{t^k}{k!} + A\sin(\omega_s t + \phi_1) \qquad (61)$$

where t is the time in the detector frame of reference, t' is the time at Solar system barycenter and ω_s is the angular frequency corresponding to Earth sidereal rotation period. All other coefficients were fitted.

For each point in the sky the entire set of timestamps was separated in 3-day stretches, with nearby stretches overlapped by 1.5 days. Each stretch was fitted using at most cubic terms $K = 3$. The absolute worst residual maximized over all stretches and all sky points was $13.2 \, \mu s$.

A similar procedure was performed for 6-day stretches, this time increasing the number of polynomial terms to $K = 4$ and using a 3-day overlap. The absolute worst residual was $24.7 \, \mu s$.

As the typical signals studied in continuous gravitational wave searches go up to 2 kHz the precision of the fit is sufficient to apply results described in this paper.

VII. CONCLUSIONS

The question of identification of continuous wave outliers to detector disturbances is of utmost importance in separating astrophysical signals from detector artifacts.

In this paper we analyze the shape of the Fourier transform of continuous wave gravitational wave signal and present simple formulas to compute peak heights and locations arising from features in frequency evolution of gravitational wave signal.

While our focus was on understanding Fourier transform of a gravitational wave signal, the formulas and the analysis presented here can be applied to any signals of this form.

VIII. ACKNOWLEDGMENTS

[1] B. P. Abbott *et al.* (LIGO Scientific Collaboration and Virgo Collaboration), All-sky search for continuous gravitational waves from isolated neutron stars using Advanced LIGO O2 data, Phys. Rev. D **100** 024004 (2019).

[2] V. Dergachev and M. A. Papa, Sensitivity Improvements in the Search for Periodic Gravitational Waves Using O1 LIGO Data, Phys. Rev. Lett. **123**, no. 10, 101101 (2019)

[3] V. Dergachev and M. A. Papa, Results from an extended Falcon all-sky survey for continuous gravitational waves, Phys. Rev. D **101**, 022001 (2020)

[4] B. P. Abbott *et al.* (LIGO Scientific and Virgo Collaborations), First low-frequency Einstein@Home all-sky search for continuous gravitational waves in Advanced LIGO data, Phys. Rev. D **96**, no. 12, 122004 (2017)

[5] B. P. Abbott *et al.* (LIGO Scientific Collaboration and Virgo Collaboration), Full Band All-sky Search for Periodic Gravitational Waves in the O1 LIGO Data, Phys. Rev. D **97** 102003 (2018).

[6] V. Dergachev, M. A. Papa, Results from the first all-sky search for continuous gravitational waves from small-ellipticity sources, Phys. Rev. Lett. **125**, 171101 (2020)

[7] B. Steltner, M. A. Papa, H.-B. Eggenstein, B. Allen, V. Dergachev, R. Prix, B. Machenschalk, S. Walsh, S. J. Zhu, S. Kwang, Einstein@Home all-sky search for continuous gravitational waves in LIGO O2 public data, arXiv:2009.12260

[8] R. Brito, S. Ghosh, E. Barausse, E. Berti, V. Cardoso, I. Dvorkin, A. Klein and P. Pani, Gravitational

wave searches for ultralight bosons with LIGO and LISA, Phys. Rev. D **96**, no. 6, 064050 (2017)

[9] M. Baryakhtar, R. Lasenby, M. Teo, Black Hole Super-radiance Signatures of Ultralight Vectors, Phys. Rev. D **96**, 035006s (2017)

[10] A. Arvanitaki, M. Baryakhtar, R. Lasenby, S. Dimopoulos, S. Dubovsky, Black Hole Mergers and the QCD Axion at Advanced LIGO, Phys. Rev. D **95**, 043001 (2017)

[11] A. Arvanitaki, M. Baryakhtar, X. Huang, Discovering the QCD Axion with Black Holes and Gravitational Waves, Phys. Rev. D **91**, 084011 (2015)

[12] C. J. Horowitz and S. Reddy, Gravitational Waves from Compact Dark Objects in Neutron Stars, Phys. Rev. Lett. **122**, no. 7, 071102 (2019)

[13] C. J. Horowitz, M. A. Papa and S. Reddy, Gravitational waves from compact dark matter objects in the solar system, arXiv:1902.08273

[14] On blind searches for noise dominated signals: a loosely coherent approach, V. Dergachev, Class. Quantum Grav. **27**, 205017 (2010).

[15] Loosely coherent searches for sets of well-modelled signals, V. Dergachev, Phys. Rev. D **85**, 062003 (2012)

[16] Loosely coherent searches for medium scale coherence lengths, V. Dergachev, `https://arxiv.org/abs/1807.02351` arXiv:1807.02351

[17] Advanced LIGO, J. Aasi *et al.* (LIGO Scientific Collaboration), Class. Quantum Grav. **32** 7 (2015) `https://iopscience.iop.org/article/10.1088/0264-9381/32/7/074001/pdf` (URL provided because PRD database keeps confusing this paper with paper on Enhanced LIGO)

[18] Efficient Estimation of Barycentered Relative Time Delays for Distant Gravitational Wave Sources, O. Sauter, V. Dergachev, K. Riles, Phys. Rev. Lett. **99**, 044006 (2019)

[19] LIGO Scientific Collaboration, LIGO Algorithm Library - LALSuite, doi:10.7935/GT1W-FZ16, 2018